The Astrophysical Journal Supplement Series, 229:16 (14pp), 2017 March https://doi.org/10.3847/1538-4365/aa5830


# A New MHD-assisted Stokes Inversion Technique

T. L. Riethmüller[1], S. K. Solanki[1,2], P. Barthol[1], A. Gandorfer[1], L. Gizon[1,3], J. Hirzberger[1], M. van Noort[1], J. Blanco Rodríguez[4], J. C. Del Toro Iniesta[5], D. Orozco Suárez[5], W. Schmidt[6], V. Martínez Pillet[7], and M. Knölker[8]
[1] Max-Planck-Institut für Sonnensystemforschung, Justus-von-Liebig-Weg 3, D-37077 Göttingen, Germany; riethmueller@mps.mpg.de
[2] School of Space Research, Kyung Hee University, Yongin, Gyeonggi, 446-701, Korea
[3] Institut für Astrophysik, Georg-August-Universität Göttingen, Friedrich-Hund-Platz 1, D-37077 Göttingen, Germany
[4] Grupo de Astronomía y Ciencias del Espacio, Universidad de Valencia, E-46980 Paterna, Valencia, Spain
[5] Instituto de Astrofísica de Andalucía (CSIC), Apartado de Correos 3004, E-18080 Granada, Spain
[6] Kiepenheuer-Institut für Sonnenphysik, Schöneckstr. 6, D-79104 Freiburg, Germany
[7] National Solar Observatory, 3665 Discovery Drive, Boulder, CO 80303, USA
[8] High Altitude Observatory, National Center for Atmospheric Research, P.O. Box 3000, Boulder, CO 80307-3000, USA
*Received 2016 July 20; revised 2016 November 14; accepted 2016 November 15; published 2017 March 22*

## Abstract

We present a new method of Stokes inversion of spectropolarimetric data and evaluate it by taking the example of a SUNRISE/IMaX observation. An archive of synthetic Stokes profiles is obtained by the spectral synthesis of state-of-the-art magnetohydrodynamics (MHD) simulations and a realistic degradation to the level of the observed data. The definition of a merit function allows the archive to be searched for the synthetic Stokes profiles that best match the observed profiles. In contrast to traditional Stokes inversion codes, which solve the Unno–Rachkovsky equations for the polarized radiative transfer numerically and fit the Stokes profiles iteratively, the new technique provides the full set of atmospheric parameters. This gives us the ability to start an MHD simulation that takes the inversion result as an initial condition. After a relaxation process of half an hour solar time we obtain physically consistent MHD data sets with a target similar to the observation. The new MHD simulation is used to repeat the method in a second iteration, which further improves the match between observation and simulation, resulting in a factor of 2.2 lower mean $\chi^2$ value. One advantage of the new technique is that it provides the physical parameters on a geometrical height scale. It constitutes a first step toward inversions that give results consistent with the MHD equations.

*Key words:* magnetohydrodynamics (MHD) – Sun: magnetic fields – Sun: photosphere – techniques: polarimetric – techniques: spectroscopic

*Supporting material:* animation

## 1. Introduction

In recent decades, many insights into photospheric processes have been retrieved from spectropolarimetric observations, mainly in the visible and near-infrared spectral range. Progress in this field was not only attained by the availability of ever larger telescopes (with an improved spatial resolution) or by going above the Earth's disturbing atmosphere, but also by advancements in the analysis techniques. While in the early years of spectropolarimetric observations the physical parameters of the solar atmosphere (temperature, magnetic field vector, line-of-sight (LOS) velocity, pressure, density and their height dependence) were directly derived from the Stokes profiles (classical estimates, see, e.g., Solanki 1993 for an overview), over the last approximately 25 years the usage of Stokes inversion techniques has become established. Initially the Milne–Eddington approach (involving height-independent atmospheric parameters; see, e.g., Harvey et al. 1972; Auer et al. 1977; Borrero et al. 2014) was most widely used, but with time (and increasing computing power) inversion codes that numerically solve the full radiative transfer equations became increasingly important. Prominent examples of such codes are the SIR code (Stokes Inversion based on Response functions; Ruiz Cobo & del Toro Iniesta 1992) and the SPINOR code (Stokes-Profiles-INversion-O-Routines; Frutiger 2000; Frutiger et al. 2000), which assume local thermodynamic equilibrium (LTE), or the NICOLE code (Non-LTE Inversion COde using the Lorien Engine; Socas-Navarro et al. 2000, 2015), which also considers non-LTE conditions.

A Stokes inversion is an iterative process that needs a first guess of the atmospheric parameters, which can be obtained from model calculations, from older results retrieved from similar targets, or in case of the magnetic field vector can also be simply constant with height, or random. The Unno–Rachkovsky equations for polarized radiative transfer (Unno 1956; Rachkovsky 1962a, 1962b, 1967) are numerically solved for the initial atmosphere, which provides the first guess of the synthetic Stokes profiles. These are then compared with observed Stokes profiles. Differences between the two sets of profiles are used to systematically change the initial atmosphere. This fitting process is iteratively repeated until a good match between the synthetic and observed Stokes profiles is reached. Finally, after multiple iterative steps, the atmosphere that leads to the best fit is considered as the best representation of the real Sun (within the limitations of the model) and is output as the result of the Stokes inversion.

Before the observed Stokes profiles can be compared with the synthetic profiles, the latter need to be degraded with all the instrumental effects that were present during the observation. A convolution of the synthetic Stokes profiles with the spectral transmission profile of the used instrument (or its approximation by fitting the macroturbulent velocity) is standard in nearly all inversion codes. Such a transmission profile can be obtained, e.g., by a laboratory measurement as part of the instrument calibration, or by a comparison of measured spectra

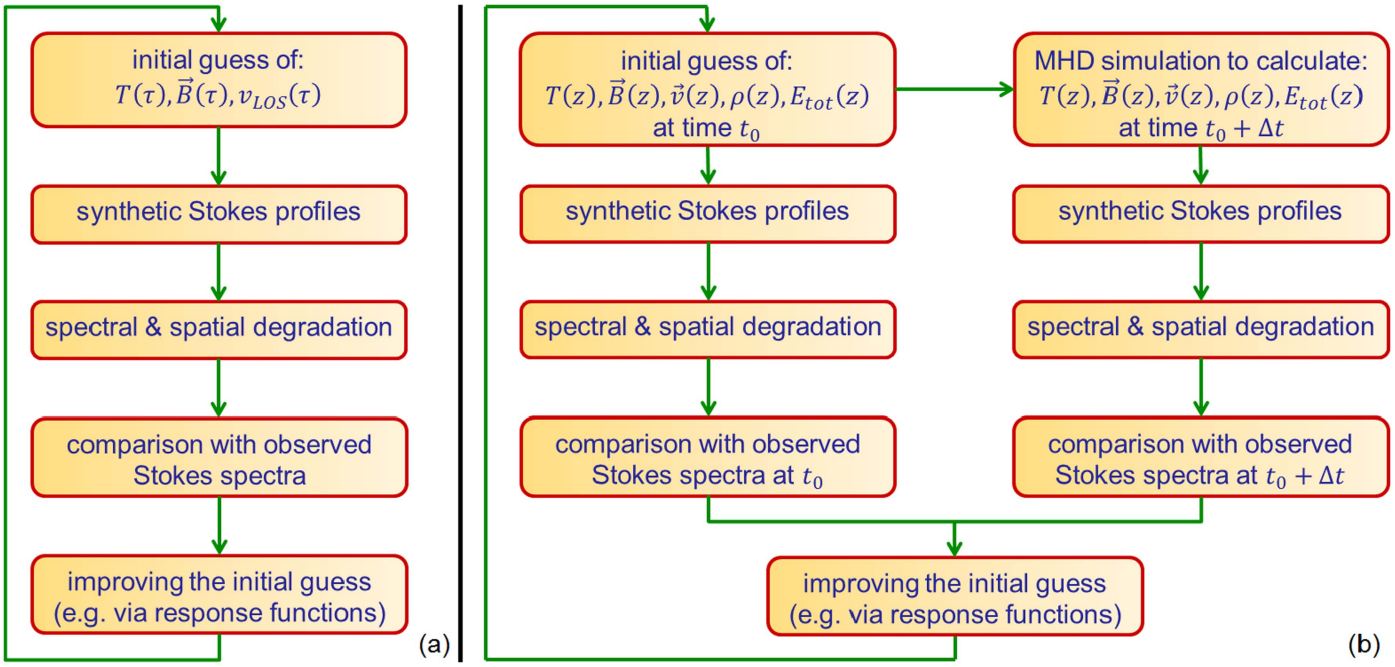


**Figure 1.** Panel (a): flow chart of the iterative fitting process of the spatially coupled Stokes inversion (van Noort 2012). Panel (b): flow chart of a hypothetical inversion process that includes the magnetohydrodynamics equations. See the main text for details.

with spectrally highly resolved spectra unaffected by spectral stray light (e.g., spectra recorded with the Fourier Transform Spectrometer; see Bianda et al. 1998; Allende Prieto et al. 2004).

A further improvement in the quality of the inversion results could be achieved by considering the spatial degradation, which introduces a spatial coupling between the pixels of a data set. Such spatial degradations can be described by the spatial point-spread function (PSF) of the instrument that can either be measured, e.g., via the phase-diversity (PD) technique (Gonsalves & Chidlaw 1979; Paxman et al. 1992; Martínez Pillet et al. 2011), modeled from the telescope geometry (e.g., Danilovic et al. 2008), or determined from an eclipse or a transit of Mercury or Venus (e.g., Wedemeyer-Böhm 2008; DeForest et al. 2009; Mathew et al. 2009). The Stokes images can then be deconvolved with the spatial PSF prior to inversions (e.g., DeForest et al. 2009; Beck et al. 2011), which regularly lowers the signal-to-noise ratio (e.g., in case of the SUNRISE/IMaX data by a factor of three, see Martínez Pillet et al. 2011). In recent years methods were developed to avoid the increase in noise by considering the spatial PSF not prior to, but during, the inversion process.

van Noort (2012) extended the Stokes inversion code SPINOR by convolving the synthetic Stokes images with a given spatial PSF before the comparison with the observations (see panel (a) of Figure 1). Since this approach strictly avoids any deconvolution, the increase of noise can be avoided to a large extent. Data recorded with the spectropolarimeter (SP) onboard the *Hinode* satellite (Tsuneta et al. 2008; Lites et al. 2013) were then successfully used to apply the spatially coupled SPINOR code (e.g., Riethmüller et al. 2013; Tiwari et al. 2013; van Noort et al. 2013; Lagg et al. 2014; Buehler et al. 2015). Ruiz Cobo & Asensio Ramos (2013) introduced another approach that decomposes the Stokes profiles into their principal components, which was later applied to quiet-Sun data recorded with *Hinode*/SP (Quintero Noda et al. 2015). It begs the question of what further improvements of the Stokes inversion technique appear possible.

Since the dynamics and evolution of the Sun are of particular interest, often observation data sets consist not only of individual snapshots at isolated points in time, but of time series. The temporal evolution of the plasma in the solar photosphere can be well described by the equations of magnetohydrodynamics (MHD), so that two consecutive observations of a time series (separated by a sufficiently small interval of time, $\Delta t$) are not statistically independent of each other, but are coupled by the MHD equations (including the equation of energy transfer). We expect that an inclusion of the MHD equations in the Stokes inversion of a time series will significantly improve the results, because a model that combines the radiative transfer equations with the MHD equations contains more physics and hence has a higher chance of approaching the real Sun.

Panel (b) of Figure 1 demonstrates how the MHD equations can be connected with a Stokes inversion. The process starts with the determination of an initial guess of the atmospheric parameters for an observation recorded at time $t_0$. In contrast to a traditional Stokes inversion, the initial guess comprises additional quantities (horizontal velocities, plasma density, and total energy) and has to be given on a geometrical height ($z$) scale, since this is the natural scale of the MHD equations (instead of an optical depth ($\tau$) scale). The extended set of atmospheric parameters allows the calculation of the temporal evolution of the plasma via an MHD code up to $t_0 + \Delta t$, which is the observation time of the next frame of the time series. After a conversion from the geometrical height into optical depth, a subset of the atmospheric parameters is used to calculate synthetic Stokes profiles, which then can be spectrally and spatially degraded. The left branch of the flow chart in panel (b) of Figure 1 illustrates this for the observation recorded at time $t_0$, while the right branch does it for the next frame recorded at time $t_0 + \Delta t$. A systematic change of the

atmospheric parameters tries to minimize the deviation of the synthetic Stokes profiles from the observed ones (for both time steps, $t_0$ and $t_0 + \Delta t$) in an iterative fitting process.

The extension of the atmospheric parameters from five to nine quantities together with the change to a geometrical height scale (of typically hundreds of grid points instead of just a few optical depth nodes), as well as the need for the relatively slow MHD simulations make the computational effort of a complete integration of the MHD equations into the Stokes inversion orders of magnitude higher than present computational capabilities. An implementation of the algorithm as shown in panel (b) of Figure 1 is hence not yet possible.

This work describes the very first approach toward the full spatially and temporally coupled inversion of spectropolarimetric observations of the solar photosphere, using MHD simulations and the PSF to link the temporal and spatial information. Section 2 explains the used observations, and Section 3 the employed MHD simulations. The method itself is outlined in Section 4, while in Section 5 we summarize and discuss the results we have achieved so far.

## 2. Observations

The observations used in this study were recorded in June 2013 during the second stratospheric flight of the balloon-borne solar observatory SUNRISE. We refer to Barthol et al. (2011) for technical details of the telescope and the gondola. Solanki et al. (2017) give an overview of the updates applied to the second flight. Image stabilization, correlation tracking, and real-time sensing of the lower wavefront aberrations were realized by a Shack–Hartmann wavefront sensor that also controlled the telescope's focus mechanism (Berkefeld et al. 2011).

Two science instruments were operated in parallel onboard SUNRISE: the SUNRISE Filter Imager (SuFI; Gandorfer et al. 2011) to record broadband filtergrams in the violet and near-ultraviolet spectral range (214–397) nm and the Imaging Magnetograph eXperiment (IMaX; Martínez Pillet et al. 2011) for spectropolarimetric observations in the Fe I 525.02 nm line. This spectral line has a Landé factor $g = 3$ and is one of the most Zeeman-sensitive lines in the visible spectrum. An overview of the recorded data is given by Solanki et al. (2017). In this study we refer to an observation recorded by the IMaX instrument on 2013 June 12, 23:39 UT. The telescope pointed to the active region AR 11768 close to the disk center (with cosine of the heliocentric angle $\mu = 0.93$). IMaX was operated in the V8-4 mode, i.e., the full Stokes vector was measured at eight wavelength positions (seven within the spectral line at $(-12, -8, -4, 0, +4, +8, +12)$ pm and one in the continuum at $+22.7$ pm offset from the line core) where four images of 250 ms exposure time were accumulated at a time. The plate scale of IMaX was $0\farcs0545$ per pixel.

In the post-processing of the IMaX data, corrections for dark current and flat-field effects were applied. A pre-flight polarimetric calibration provided a Müller matrix for each pixel of the field of view (FOV) that allowed a removal of the instrumental polarization (Martínez Pillet et al. 2011). Because the primary mirror could not be included in the polarimetric calibrations, and because the thermal environment was different during the observations than during calibration, the elements of the Müller matrices slightly changed, which we took into account by applying an ad hoc cross-talk removal of the order of 1%. The thus reduced data are named level-1 (or non-reconstructed data).

A PD measurement was achieved about two hours before the observation by inserting a PD plate into the optical path of one of the two IMaX cameras. This allowed the retrieval of a PSF used to correct the data for low-order wavefront aberrations (Gonsalves & Chidlaw 1979; Paxman et al. 1992). The PD reconstructed data are named level-2. More details are reported by Martínez Pillet et al. (2011). See also Solanki et al. (2017) for additional details concerning data reduction steps specific to IMaX during the second SUNRISE flight.

## 3. Simulation and Spectral Synthesis

We accomplished realistic simulations of the radiative and MHD processes in the solar photosphere and upper convection zone with the MURaM (Max Planck Institute for Solar System Research/University of Chicago Radiation Magneto-hydrodynamics) code, a three-dimensional, non-ideal, compressible MHD code that includes non-gray radiative transfer calculations in the energy equation under the assumption of local thermal equilibrium (Vögler et al. 2005). The simulation box is 24 Mm × 24 Mm in its horizontal dimensions and has a depth of 6.1 Mm. The cell size of the simulation box is 41.7 km in the two horizontal directions and 16 km in the vertical direction.

We used a statistically relaxed purely hydrodynamical simulation as the initial condition. A homogeneous unipolar vertical magnetic field of $\langle B_z \rangle = 400$ G was then introduced into the hydrodynamical simulation and the simulation run was continued for another three hours of solar time to reach again a statistically relaxed state. After the relaxation a single snapshot covering several pores with field strengths up to 3500 G (at $\log(\tau) = -1$) is used for this study; see the left panel of Figure 2. The boundary conditions were periodic in the horizontal directions and closed at the top boundary of the box, while a free in- and outflow of plasma was allowed at the bottom boundary under the constraint of total mass conservation. The $\tau = 1$ surface for the continuum at 500 nm was on average reached about 700 km below the upper boundary.

The forward calculation mode of the SPINOR inversion code (Solanki 1987; Frutiger 2000; Frutiger et al. 2000) was used to compute synthetic Stokes spectra of the Fe I 525.02 nm line used by IMaX. We synthesized the strongest 20 spectral lines in the range (524.72–525.32) nm whose atomic parameters are listed in Riethmüller et al. (2014). The radiative transfer was calculated for a heliocentric angle of $\mu = 0.93$.

## 4. Method

### 4.1. Concept

In this section we present an alternative method to obtain the atmospheric parameters from observed Stokes profiles, i.e., an alternative to the traditional Stokes inversion technique purely based on radiative transfer calculations and the computation of a model atmosphere assuming hydrostatic equilibrium (usually restricted to the vertical direction). The idea is to use an MHD simulation of a target similar to the observations (in our case pores and granulation) for a Stokes synthesis of the observed spectral range. The synthetic Stokes data then have to be adapted to the pixel size of the observation and degraded with all the instrumental effects that influenced the observational data. To gain a comprehensive knowledge about these instrumental effects is possibly the greatest difficulty of the method.

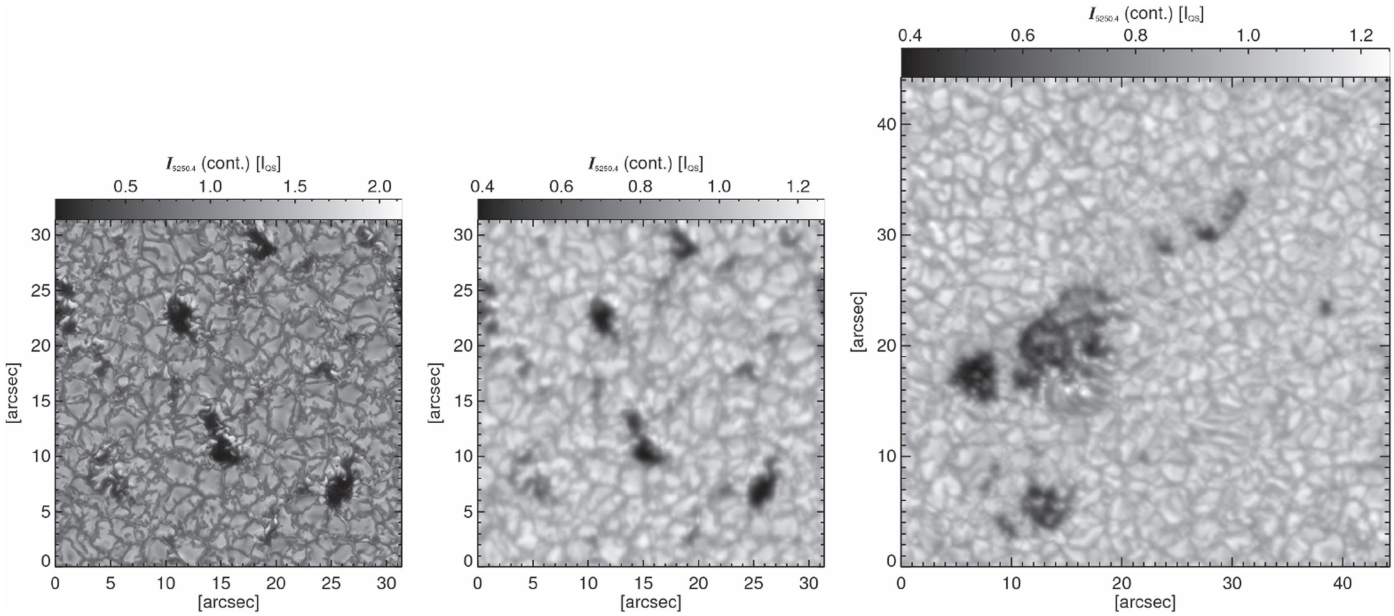


**Figure 2.** Images of the Stokes $I$ continuum at 525.04 nm, normalized to the mean quiet-Sun intensity, $I_{QS}$. The left panel displays the original (i.e., undegraded) MHD data, the middle panel displays the fully degraded MHD data, and the right panel displays the level-1 IMaX observation.

We now consider the degraded MHD data set as a pool of Stokes profiles that can be directly compared with the observed profiles. In a first iteration, a pixel in the degraded data set is assigned to a particular observed pixel, namely the one that shows the least deviation between observed and synthetic Stokes profiles. The assigned MHD pixels embody the inversion result of the first iteration.

Our inversion result (a pixel in the degraded MHD data set) is not only connected to the temperature, magnetic field vector, and LOS velocity in the photosphere as is the case for results of traditional Stokes inversion techniques, but also the full set of undegraded MHD data is available, including horizontal velocities and also including information on the layers immediately below the solar surface, which are not directly accessible via spectral lines. Because the layers below the solar surface drive the features at this surface, the inversion of a time series of Stokes data has the potential to constrain the subsurface dynamics. The stratifications of the atmospheric parameters obtained by our inversion method are available on a geometrical height scale, while traditional Stokes inversions usually provide an optical depth scale, whose conversion into geometrical heights is influenced by the underlying assumptions (see, e.g., Puschmann et al. 2010).

While the method up to this point has already been considered by other authors in a more or less similar way (Molowny-Horas et al. 1999; Tziotziou et al. 2001; Berlicki et al. 2005; Carroll & Kopf 2008; Beck et al. 2013b, 2015), we go a step further and re-sort the MHD data set according to the best-fit results (see Section 4.4) and use the re-sorted data as the initial condition of a new MURaM simulation (see Section 4.5). The re-sorting takes a physically consistent simulation box and produces a physically inconsistent one out of it, e.g., the horizontal flow pattern and the magnetic field lines are destroyed by the rearranging. During a relatively short relaxation process the MURaM code removes the physical inconsistencies (in the same way as when the 400 G were artificially introduced, see Section 3) and we obtain MHD data that are very similar to the observation.

While we only require from the original MHD simulation that it contain granulation and pores of any size and shape, the new simulation shows pores having sizes, shapes, and positions within the FOV that are similar to the observation. The better an MHD simulation matches the observation, the better the fitting of Stokes profiles can work, so that a significant improvement of the results can be reached by repeating the method iteratively, i.e., the new MHD simulation is used as input for a second iteration of spectral synthesis, degradation, Stokes profile fitting, and MHD simulation.

We name the new technique MHD-asssisted Stokes Inversion (MASI).

### 4.2. Degradation of the MHD Data

As mentioned in Section 2, we have the choice between non-reconstructed and reconstructed observations. The reconstruction is done with a spatial PSF determined by in-flight PD measurements which provide the low-order aberrations of the telescope (defocus, coma, astigmatism, etc.), i.e., aberrations that determine the inner core of the PSF. The PD measurements do not (or hardly) provide information on high-order aberrations which determine the wings of the PSF, e.g., the stray-light behavior of the system.

Only if the degradation of the synthetic data reflects the real situation in the observed data to a high degree is a physically meaningful comparison between them possible. From the higher quality of the reconstructed data it is clear that a comparison with the non-reconstructed data requires a stronger degradation than a comparison with reconstructed data. Because deconvolution of the data with the PD PSF is not a straightforward procedure, we demonstrate our new inversion technique with non-reconstructed data. This is to strictly avoid any deconvolution of the observations. In the following we depict all steps needed to degrade the synthetic data to the level of the non-reconstructed observations (level-1).

#### 4.2.1. Spectral Resolution and Sampling

The spectral PSF of IMaX was measured in the laboratory before the launch of SUNRISE (see the bottom panel of Figure 1 in Riethmüller et al. 2014) and considers not only the transmission behavior of the etalon but also the used pre-filter. In addition to the 6.5 pm wide primary peak, the spectral PSF also shows secondary peaks at around ±200 pm offset from the position of the transmision maximum. In order to include the possible influence of the secondary peaks we synthesize all the 20 spectral lines we could identify in the ±300 pm range around 525.02 nm.

The synthetic Stokes profiles are convolved with the spectral PSF in order to reproduce the spectral resolution of IMaX. Finally, Stokes images are created for the spectral range −15 pm to +30 pm in spectral steps of 1 pm, because such two-dimensional Stokes images are needed for a convolution with a spatial PSF such as the one we apply in the following degradation step. The chosen spectral sampling of 1 pm is a reasonable compromise between the amount of data and the spectral resolution. The chosen spectral range is a little wider than the scanning range of IMaX in its V8-4 mode (−12 pm to +22.7 pm) because of the blueshift effect inherent in IMaX, which will be explained in Section 4.4.

#### 4.2.2. Diffraction Limit and Low-order Aberrations

As mentioned above, the diffraction at the telescope 1 m aperture and the low-order wavefront aberrations were measured by IMaX during the flight via the phase-diversity technique. Consequently, the synthetic Stokes images were convolved with the spatial PSF retrieved from the PD data to take these effects into account.

#### 4.2.3. Residual Jitter

Besides the 1 m aperture of the telescope at the considered wavelength, the spatial resolution of SUNRISE was limited by the stability of the image. The pointing system stabilized the gondola to an accuracy of a few arcseconds, while the Correlating Wave-Front Sensor (CWS) controlled a tip/tilt mirror so that the reflected beam was further stabilized down to an rms value of only 0.″025 (measured during the flight by the CWS). Applying an artificial jitter of that strength to the MHD images led to significantly less image smearing than seen in the IMaX observations. A possible, but speculative, explanation could be a differential motion between the CWS camera and the IMaX cameras. All cameras are located within the post-focus-instrumentation (PFI) structure, that is made of carbon fiber and was designed for high stiffness. Nonetheless, with an F/121 beam inside the Image Stabilization and Light Distribution System (ISLiD; Gandorfer et al. 2011) even a minute bending (due to vibrations) would suffice to explain the IMaX image quality.

In order to take the actual image smearing into account we decided to apply a combination of two Butterworth lowpass filters (one with a low cut-off frequency, the other with a much higher one; Butterworth 1930) because it degraded the MHD data slightly more realistically than a convolution with a two-dimensional Gaussian (as we applied to data from the first SUNRISE flight in Riethmüller et al. 2014), in particular with respect to the power spectrum.

#### 4.2.4. Stray Light

A reliable determination of the stray-light properties of SUNRISE is a challenge since they strongly influence the data (in particular the rms intensity contrast) but are difficult to measure. Riethmüller et al. (2014) assessed the stray-light contamination of the first flight IMaX data from analyzing observations of the solar limb. Unfortunately, during the second flight the limb was only observed in the late phase of the mission when IMaX had problems with the electronics stabilizing the etalon temperature.

The limb data contain clear evidence for a non-local stray-light contamination, i.e., that the stray-light PSF has extended wings. Additionally, we can distinguish between two stray-light sources: The light level seen at the image border not exposed to sunlight (the border is caused by the field stop at the entrance of the IMaX instrument) can only be caused by IMaX internal stray light, while the somewhat higher total stray-light level in the off-limb region of the images indicates a second, albeit smaller, contribution coming most probably from outside IMaX. Unfortunately, we cannot use the limb data for a more quantitative assessment of the stray-light properties because of the floating etalon temperature and also because the correlation tracker had problems in stabilizing the image in the direction parallel to the solar limb, making these images less sharp than those on the disk.

During the SUNRISE calibration on the ground, a fiber bundle was placed in the secondary focal plane, F2. The fiber bundle is an extended light source with a diameter of about 8.″5 centered in the 51″ × 51″ IMaX FOV making this a nearly ideal target to determine the stray-light properties of IMaX. An illumination with sunlight was not possible for technical reasons so an artifical light source (75 W xenon lamp) had to be used. All frames of the fiber-bundle calibration campaign were summed up. The summed image was then deconvolved with the ideal (i.e., stray-light and aberration free) fiber-bundle image approximated by a binary mask image retrieved by applying an intensity threshold to each fiber of the summed fiber-bundle image. The deconvolution was done via the Lucy–Richardson algorithm (Richardson 1972; Lucy 1974) which is an iterative method that uses only convolutions. Compared to the Sun, the light level of the used artifical light source was extremely low, leading to a low signal-to-noise ratio in the outer parts of the fiber-bundle images. Hence the stray-light related far wings of the PSF could not be retrieved with the required accuracy.

Even if these attempts in measuring the stray-light PSF did not yield a result that could be directly used, they helped to considerably narrow down the shape of the azimuthally averaged PSF. From this we could determine that the stray light seen by IMaX has neither a purely local nor a purely global character, but that the influence of stray light on every spatial scale is present.

Since the stray-light PSF could not be determined with adequate accuracy, only the utilization of a simplistic stray-light model remains. We contaminate the synthetic Stokes $I$ images with 25% global stray light.[9] Stokes $Q$, $U$, $V$ are not contaminated because most of the stray light was created internally inside IMaX and the internal stray light is largely unpolarized.

[9] Contamination with 25% global stray light means that a subtraction of 25% of the spatial mean Stokes profile from the individual contaminated profiles results in the original (stray-light free) profiles.

The above strength of the global stray light was tested by a test-wise inversion of the IMaX data carried out with the traditional SPINOR code and in particular by evaluating the resulting magnetic field maps. A simple and hence robust atmospheric model was used: three $\log(\tau)$ nodes for the temperature; everything else was assumed to be height-independent. Without any stray-light correction the inversion provided kilogauss fields mainly along the edges of pores, and unrealistic weaker fields in the centers of the pores. This effect can be explained by the broad wings of the stray-light PSF. Inside the pores the low temperatures together with the shallow temperature gradients led to low intensities and extremely small line depths of the 525.02 nm spectral line, so that contamination with light from the bright vicinity of the pores caused a significant underestimation of the field strength. A global stray-light correction of the data lowered this effect considerably. The best results could be reached for a stray-light strength of 25%.

Two other methods, which are independent of the field weakening in the pores, confirmed that a 25% of global stray-light together with the Butterworth filtering is reasonable. First, the intensity of the darkest pixel in the synthetic pores in the MHD simulations increases from 8.6% to 38.8% of the mean quiet-Sun intensity, $I_{\rm QS}$, when the various degradation steps described above are applied. This value agrees nicely with the minimum intensity of the non-reconstructed IMaX data, 38.4%. We note that the size of the largest pore in the MHD data is smaller than in the IMaX data, which possibly makes the comparison of the minimum intensities problematic, but later in this study we will see that the match also holds if the IMaX data are compared with simulations of nearly identical pore sizes. Second, the rms contrast of the Stokes $I$ continuum image of the non-reconstructed IMaX data, 6.8%, is similar to the constrast of the fully degraded MHD data, 7.7% (pores were excluded when we determined these numbers).

#### 4.2.5. Noise

IMaX Stokes $Q$, $U$, and $V$ images at the continuum wavelength (+22.7 pm) were used to calculate histograms of a quiet-Sun region, which is generally free of polarization signals. The histograms showed a clear Gaussian shape with a standard deviation of about $2.3 \times 10^{-3}\ I_{\rm QS}$ (level-1 data) or $7 \times 10^{-3}\ I_{\rm QS}$ (level-2 data), respectively. $I_{\rm QS}$ is the mean continuum intensity of the selected quiet-Sun region. We did not add any noise to the synthetic data to avoid complicating the comparison with the observations, but we used the standard deviation as the noise value for all four Stokes parameters when calculating the $\chi^2$ values of the merit function we define in Equations (1) and (2).

### 4.3. Assessment of the Degradation

Since our method relies on a direct comparison between degraded synthetic and observed Stokes profiles (see also Danilovic et al. 2010; Beck et al. 2013a; Riethmüller et al. 2014), a realistic degradation is crucial. In this section we assess the quality of the degradation steps decribed in Section 4.2 by comparing the two data sets. In our experience it is important that not just a single quantity (e.g., the rms intensity contrast) is compared but multiple ones. In practice, the measurement of instrumental effects might not be possible with the necessary accuracy, so those effects often need to be approximated by simplified models (in our case stray light and jitter) containing one or more adjustable parameters.

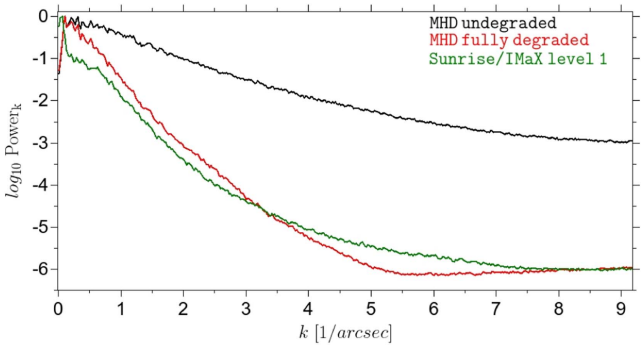


**Figure 3.** Logarithm of the azimuthally averaged power spectra of the Stokes $I$ continuum images vs. the wave number, $k$. The black line corresponds to the undegraded MHD simulation, the red line to the fully degraded data, and the green line displays the level-1 IMaX observation.

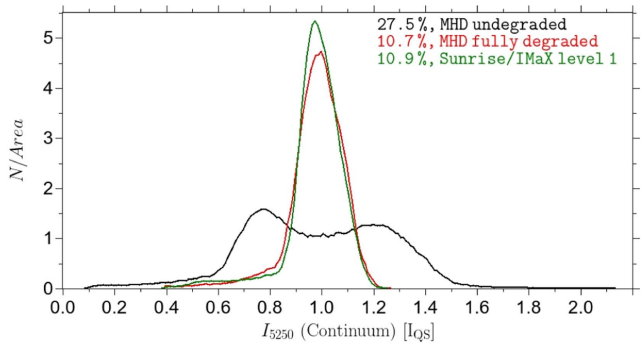


**Figure 4.** Histograms of the normalized Stokes $I$ continuum intensity. The color coding is the same as in Figure 3. rms contrasts are indicated in the text labels. The histograms cover the full FOV, i.e., the pores are included.

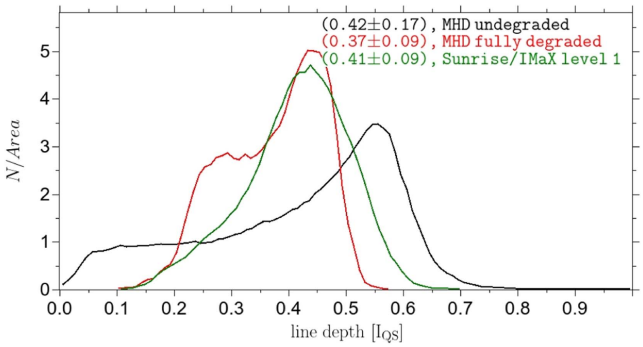


**Figure 5.** Same as Figure 4, but for the Stokes $I$ line depth. Mean values and their standard deviations are indicated in the text labels.

Figure 2 exhibits the influence of the degradation on the synthetic Stokes $I$ continuum image and compares the undegraded and degraded synthetic images with the corresponding IMaX observation. The degradation clearly lowers the contrast and the spatial resolution so that the image quality of the synthetic data is brought down to the level of the observation.

In Figure 3 we show the azimuthally averaged power spectra (e.g., Puschmann & Beck 2011; Katsukawa & Orozco Suárez 2012) and in Figure 4 the intensity histograms both calculated from the images displayed in Figure 2. The same color coding is used for Figures 3–5: The black line corresponds to the undegraded synthetic data, the red line to

the degraded synthetic data, and the green line to the non-reconstructed IMaX observations.

A comparison of the power spectra reveals that our degradation steps bring the spectrum down to roughly the level of the observed spectrum, but some mismatch remains. For wave numbers $k < 3.5$ arcsec$^{-1}$ the synthetic power is not sufficiently suppressed by the degradation, while it is too low for higher wave numbers (see Figure 3).

The degradation of the synthetic data reduces the rms intensity contrast from 27.5% down to 10.7% which is 0.2% lower than the observational contrast of 10.9% (see Figure 4). The histograms are calculated for the full FOV, including pores. If we exclude the pores (that fill different fractions of the FOV in the two data sets) then we find the rms contrast values given in Section 4.2.4.

As mentioned above, the stray light can have a severe influence on the line depths, in particular in the pores. Hence we also show histograms of the Stokes $I$ line depth in Figure 5. While the standard deviation matches well between the degraded simulation and the observation, the mean value of the synthetic data is slightly lower than the observed value (see text labels). Additionally, the synthetic line-depth histogram exhibits a bi-modal shape which is not the case for the observed histogram.

Figures 2–5 illustrate the quality of our degradation. The remaining discrepancies can be caused by various effects, such as the uncertainties in the stray-light correction mentioned in Section 4.2.4. Additionally, the lowpass filtering with a combination of two Butterworth filters is only a very simple way of modeling the residual jitter. Although the degradation of the MHD data might not perfectly mimic the behavior of IMaX we believe it successfully accounts for the most important contributions.

### 4.4. Stokes Profile Fitting

After taking the various instrumental effects into account, we now have two data sets available that are directly comparable, except for two remaining discrepancies. The first discrepancy concerns the magnetic polarity, because our MHD simulation is a unipolar one, while both magnetic polarities are present in the IMaX observation. Hence we create a second MHD data set by flipping the sign of the magnetic field vector, while all other quantities remain unchanged. The second MHD data set is degraded in the same manner as the original one, so that a bipolar data set can be produced by combining the two opposite polarity data sets.

The second discrepancy concerns the blueshift that is the sum of the field-dependent etalon blueshift and the constant convective blueshift. The etalon blueshift is a wavelength shift across the FOV due to the inclination of the off-axis rays as they reach the etalon in a collimated configuration. The map of the total blueshift is provided by the IMaX calibration process (Martínez Pillet et al. 2011).

For the traditional Stokes inversion method the velocity map needs to be corrected for the blueshift just at the very end. In the MASI case the blueshift has to be taken into account directly during the fitting of the observed Stokes profiles.

Consider now a given pixel of the observation data. Its position within the FOV of IMaX determines its blueshift. This particular blueshift is subtracted from the nominal wavelengths of the V8-4 mode. Every degraded synthetic profile (which has high spectral sampling) of all pixels in the MHD FOV is then re-sampled at the corrected wavelengths, resulting in a blueshift-corrected MHD data set. We then browse through the corrected MHD data set in order to identify the pixel whose Stokes profiles match the observed one best. We assess the similarity of Stokes profiles by defining the following $\chi^2$ merit function:

$$\chi^2(x_o, y_o) = \frac{1}{32}\sum_{w=1}^{8}\sum_{s=1}^{4}\frac{(I_{w,s}^{\rm obs}(x_o, y_o) - I_{w,s}^{\rm syn}(x_m, y_m))^2}{\sigma_s^2}, \quad (1)$$

where $(x_o, y_o)$ is the pixel position within the observed FOV composed of $812 \times 812$ pixels, while $(x_m, y_m)$ is the position within the MHD FOV consisting of $1152 \times 576$ pixels. $w$ runs over the eight wavelengths of the V8-4 mode and $s$ over the four Stokes parameters, $I$, $Q$, $U$, $V$, e.g., $I_{2,1}^{\rm syn}$ means the degraded synthetic Stokes $Q$ signal at the wavelength $-4$ pm. $\sigma_s$ is the noise level of the Stokes parameter $s$.

This step of the MASI algorithm searches for the MHD pixel whose degraded Stokes profiles provide the smallest $\chi^2$ value for the given observed pixel. The position of the best-fit MHD pixel within the MHD FOV is assigned to the observed pixel. Repeating this procedure for all observed pixels needed 19 hr on a single Intel(R) Core(TM) i7-2760QM and resulted in two maps having the size of the observed FOV and giving the $x$ and $y$ coordinates of the best-fit MHD pixels (not shown). These coordinates are then used to create a new MHD data set by re-sorting the original one. The new MHD data set covers the FOV of the observation and holds for each position within the FOV the one MHD pixel that best fits the observed one at this position. We note that not all pixels of the simulation need to find their way into the re-sorted data set, whereas others may provide the best fit to multiple Stokes profiles.

Figure 6 demonstrates the re-sorting using the example of the degraded Stokes $I$ continuum image. The archive of the Stokes $I$, $Q$, $U$, and $V$ profiles calculated from the used MHD snapshot contains $2 \times 576 \times 576$ entries (see the left panel of Figure 6). 19% of the entries in the archive provide best fits to the Stokes parameters in the IMaX data set, i.e., this fraction is actually chosen by the code to build up the re-sorted data set (right panel of Figure 6), whose comparison with the IMaX observation (right panel of Figure 2) shows a remarkable match. Only the penumbra-like region around the position (15″, 14″) looks less smooth than other regions, mainly because it is composed of just a few intensity levels.

Maps of the Stokes $V$ signal at a wavelength offset by +8 pm from the line core are compared between the IMaX observation and the MASI result in Figure 7. The bipolar structure of AR 11768 is well reproduced by MASI as well as most of the magnetic fine structure. A mismatch is again found in the penumbra-like region around the position (15″, 14″) and also in the flux-emergence region around (30″, 12″) because our archive of synthetic Stokes profiles does not contain profiles of such features with a nearly horizontal magnetic field.

Another difference in the Stokes $V$ images can be found for the interior of the pores. The peripheral region of the pores is well reproduced by the first MASI iteration, while the weakening of the circular polarization in the central part of the pores differs slightly. We speculate that the discrepancy is caused by imperfections in the degradation of the data, in particular by our imperfect knowledge of the stray-light contribution to the PSF. On top of that, the equal noise levels in the calculation of the merit function lead to a certain bias

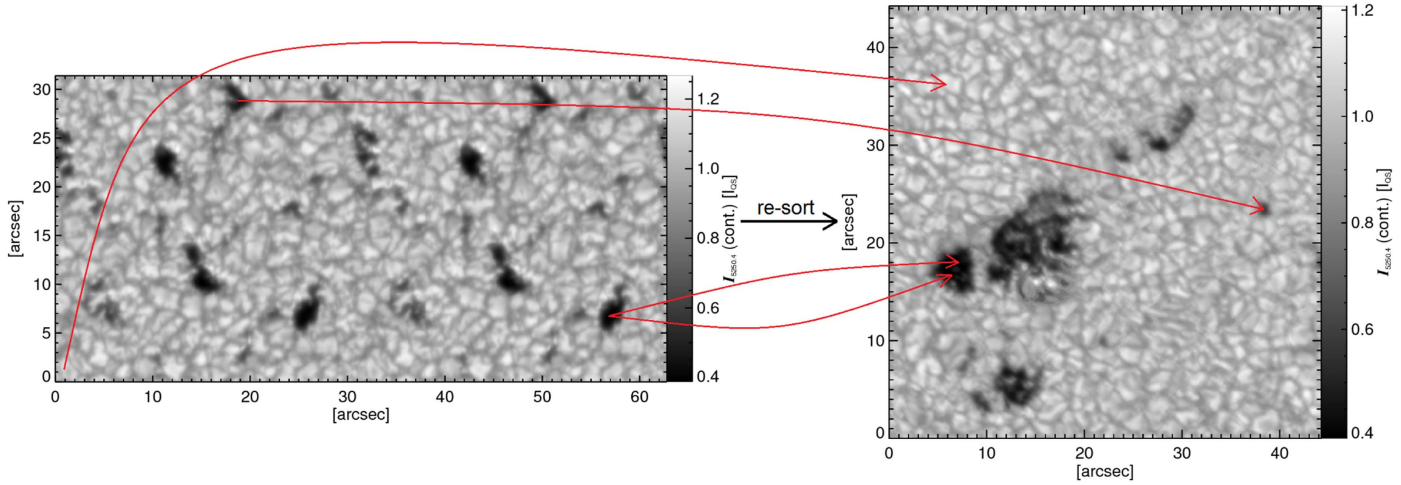


**Figure 6.** Stokes $I$ continuum image of the degraded MHD data before the re-sorting by the first iteration of the MHD-assisted Stokes Inversion (MASI) method (left panel) and afterwards (right panel). The red arrows show a few examples of the re-sorting.

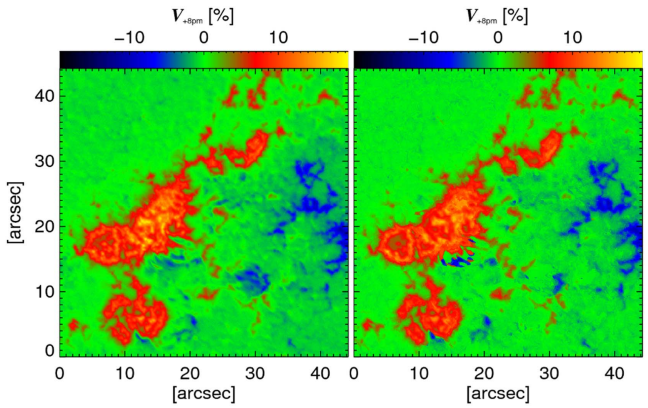


**Figure 7.** Stokes $V$ image in the red wing of the Fe I 525.02 nm line, normalized to the mean quiet-Sun intensity. Left panel: non-reconstructed data observed by IMaX. Right panel: degraded MHD data re-sorted by the first MASI iteration.

toward Stokes $I$ because the Stokes $I$ amplitude is larger then the Stokes $Q$, $U$, and $V$ amplitudes.

Panel (a) of Figure 8 shows the undegraded Stokes $I$ continuum image after the re-sorting. Its rms quiet-Sun intensity contrast of 22.5% is only slightly below the value of the undegraded MHD data before the re-sorting, 25.1% (left panel of Figure 2) but considerably larger than the contrast of the degraded image, 6.6% (right panel of Figure 6). The undegraded MASI result restores the rough topology of pores and granules quite well. However, the transition regions between granules and intergranular lanes are not very smooth but show lots of small-scale spatial discontinuities.

The quality of the MASI results relies not only on how well the MHD data are degraded but also on a good representation of the observed target types by the MHD data set. Pores and granulation are contained in our MHD simulation and hence these features can be reproduced by the MHD pixels quite well. Since the simulation does not contain any penumbra or similar features of more horizontal fields, one cannot expect good fits for the observed penumbra-like region. A look at the $\chi^2$ map (panel (b) of Figure 8) reveals the same conclusion. The largest $\chi^2$ values can be found in the penumbral region. The mean $\chi^2$ value of the first MASI iteration is 17.1, while it is 27 for a traditional SPINOR inversion of the used non-reconstructed

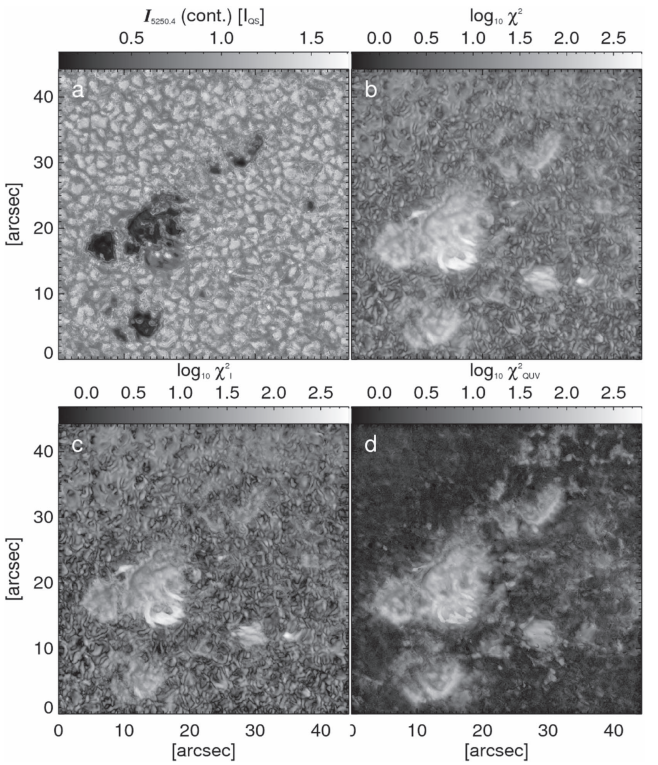


**Figure 8.** Stokes I continuum image taken from the undegraded MHD data set after the re-sorting by the first MASI iteration (panel (a)), map of the total $\chi^2$ values at the end of the first iteration of Stokes profile fitting (panel (b)), contribution of Stokes $I$ (panel (c)) and of Stokes $Q$, $U$, $V$ together (panel (d)) to the total $\chi^2$. Panels (b)–(d) are plotted on a logarithmic scale.

IMaX observation (including a 25% global stray-light correction). A decomposition of the $\chi^2$ values into contributions from Stokes $I$ (panel (c) of Figure 8) and Stokes $Q$, $U$, and $V$ together (panel (d) of Figure 8) reveals that even for the regions of more horizontal field around positions (15″, 14″) and (30″, 12″) the two contributions are of roughly the same magnitude. On average Stokes $I$ contributes 63% to the total $\chi^2$ value, while the fraction of Stokes $Q$, $U$, and $V$ together is 37%.

More details of the re-sorted MHD data will be presented after the second MASI iteration in Section 4.6.

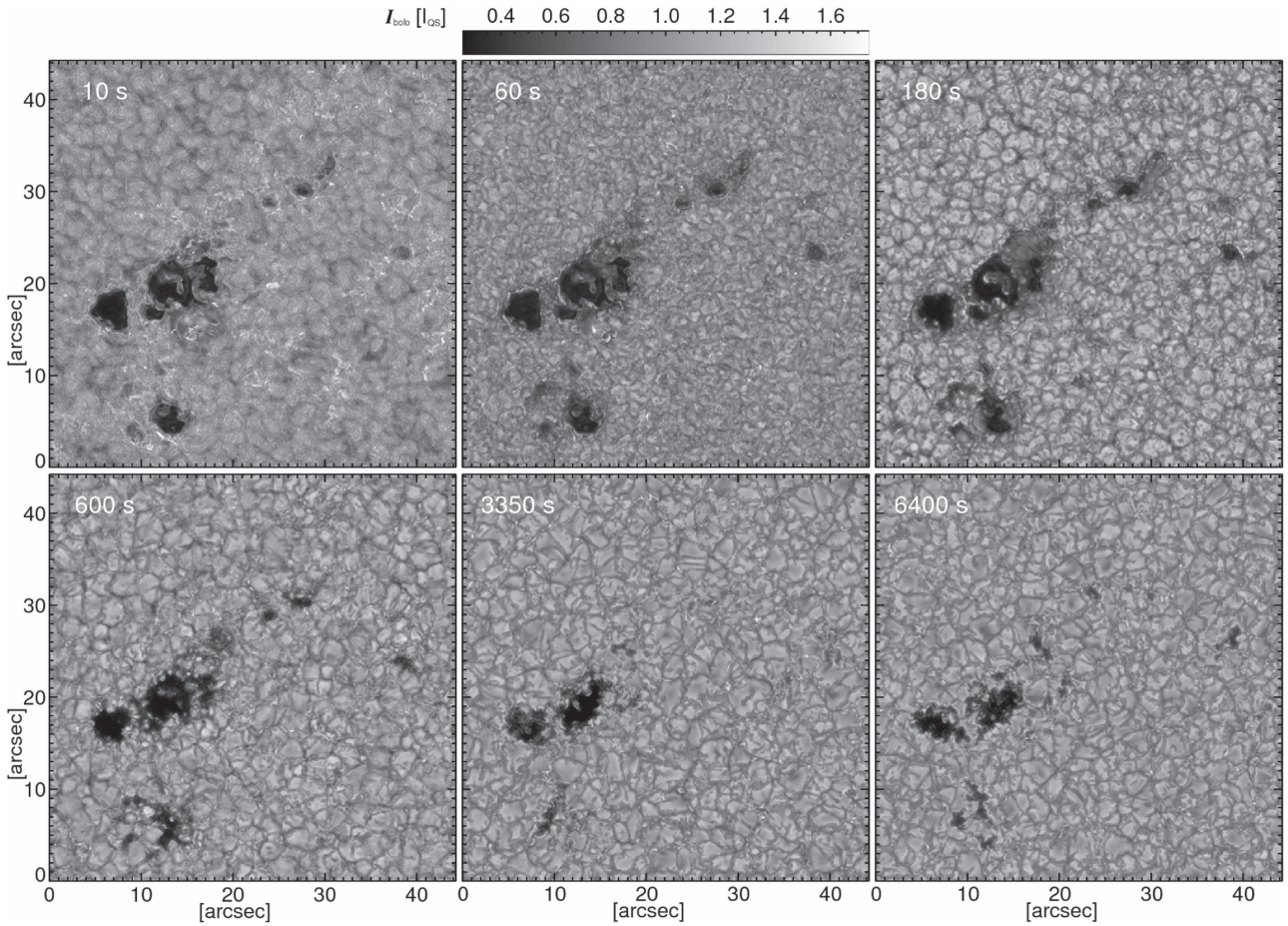


**Figure 9.** Time evolution of the bolometric intensity of a MURaM simulation using the MASI first-step results as the inital condition. We present snapshots at $t = 10$, 60, 180, 600, 3350, and 6400 s (see text labels). An animation of this figure, together with the vertical components of the velocity and magnetic field vector at optical depth unity, are provided with the online material.

(An animation of this figure is available.)

### 4.5. Continuation of the MHD Simulation

After the first step of the MASI method has been introduced and applied to an IMaX observation, and after we have presented some results, we now take the next step, which takes advantage of the availability of the entire set of MHD quantities because the re-sorting not only processes the degraded Stokes images but all available data are re-sorted. We start a new MURaM simulation that uses the first-step MASI result as the initial condition. The boundary conditions of the new run are identical to those described in Section 3. The re-sorting of the MHD data increases the horizontal dimensions of the simulation box to the size of the IMaX observation, 33.8 Mm × 33.8 Mm, while the depth of the box is kept at 6.1 Mm.

Figure 9 displays maps of the bolometric intensity for snapshots taken at 10 s, 1, 3, 10, 56, and 107 minutes of solar time after the start of the MURaM continuation (see text labels). The re-sorting of the MHD data by the MASI technique destroys important physical properties of the system, e.g., the horizontal flow pattern is arbitrarily re-sorted, the horizontal pressure balance is disturbed, and the magnetic field lines are changed by the re-sorting, so that Maxwell's equation $\nabla \cdot \boldsymbol{B} = 0$ is violated.

Even if the granulation pattern observed by IMaX is given as the initial condition, immediately after the start of the MURaM continuation the IMaX granulation pattern is destroyed, mainly caused by the unrealistic horizontal velocites. After about three minutes of solar time a new granulation pattern has evolved that is statistically similar, but looks different in detail from the IMaX granulation. The newly developed granulation pattern indicates that after approximately three minutes a new horizontal flow pattern has been established, at least in the upper layers of the convection zone.

The MURaM code is also able to re-establish the physical consistency with respect to the magnetic field. Each MURaM calculation can lead to tiny deviations from the $\nabla \cdot \boldsymbol{B} = 0$ constraint due to numerical rounding errors. Hence the code includes a $\nabla \cdot \boldsymbol{B}$ cleaning algorithm which is of great benefit for our MURaM continuation of a re-sorted MHD data set. An analysis of the temporal evolution of the $\nabla \cdot \boldsymbol{B}$ field (not shown) reveals that after 34 minutes the value has reached the normal value seen before the re-sorting.

Because on average pores live much longer than granules, their details also evolve within a few minutes but their rough shape remains unaffected for longer time. Since for stray-light analyses it might be important to work with synthetic pores of the same size as in the observations, it is interesting to mention that smaller pores (e.g., at the positions (24″, 29″), (28″, 30″), and (38″, 23″) in the right panel of Figure 2) can disappear after a while (see snapshot at $t = 3350$ s of Figure 9), but because

the magnetic flux is conserved, pores of similar sizes can reappear at similar locations (see snapshot at $t = 6400$ s).

An animation of the bolometric intensity as well as the vertical components of the velocity and magnetic field vector at optical depth unity is available.

### 4.6. Iterative Procedure

Our considerations in Sections 4.1–4.5 started with MHD data containing a solar scene that is similar to the observed scene only in the sense that it contains similar types of features. After the MHD data were degraded, they could be used for a Stokes inversion of the observation via the described method. The first iteration MASI result was a re-sorted MHD data set that was used as the initial condition of a new MURaM simulation. After about half an hour the new simulation reached a statistically relaxed state in which the horizontal flow pattern and the magnetic field lines were again in accordance with the MHD equations. That way we obtain MHD data containing a solar scene that is both physically consistent (at least in the visible layers of the Sun), and much more similar to our IMaX observations than the MHD data we started with. We now pursue the question of whether an iteration of the outlined method is able to improve the correspondence of the simulated and the observed data.

The reapplication of the method described in the following text is named the second MASI iteration. We use the snapshot at $t = 600$ s (bottom left panel of Figure 9) as the MHD data set for the second iteration because we aim for a close resemblance to the IMaX observation. In particular we are interested in the smaller pores that are difficult to treat with the traditional Stokes inversion technique. Actually one should only use snapshots taken after the relaxation process is entirely completed ($t \approx 34$ minutes), but because $\nabla \cdot \boldsymbol{B}$ drops very rapidly during the first 10 minutes after which it continues to slowly reach the value before the re-sorting after a further 24 minutes, the selected snapshot at $t = 10$ minutes strikes a reasonable balance. (We note that the smaller pores temporarily disappear for $t > 10$ minutes.) The trick of doubling the MHD data set in order to make its magnetic field bipolar is no longer needed because the snapshot at $t = 600$ s is already bipolar. Thirty hours of execution time were needed to run the MURaM code for 600 s of solar time on a cluster of 160 Intel(R) Xeon (R) cores E5-2670.

A further change in the second iteration is that we this time invert reconstructed IMaX data (level-2) via MASI in order to demonstrate that the MASI method leaves the user the choice of whether the observations are deconvolved with a PSF or the MHD data are convolved. This can be an advantage, because a deconvolution of observational data with a PSF leads regularly to a decrease in the signal-to-noise ratio, while it provides a higher spatial resolution (compare panel (a) of Figure 10 with the right panel of Figure 2). As a consequence, the convolution of the MHD data with the PD PSF is skipped this time because the PD PSF is already considered during the reconstruction of the IMaX data. All other degradation steps (convolution with the spectral PSF, Butterworth lowpass filtering, and 25% global stray-light contamination) have to be applied in the same way as for the first iteration. The rms quiet-Sun intensity contrast of the degraded synthetic Stokes $I$ continuum image, 13.67%, agrees very well with the contrast of the IMaX level-2 data, 13.25%, likewise the intensity of the darkest pixel ($0.308\, I_{\rm QS}$ for the synthetic data and $0.285\, I_{\rm QS}$ for the IMaX data).

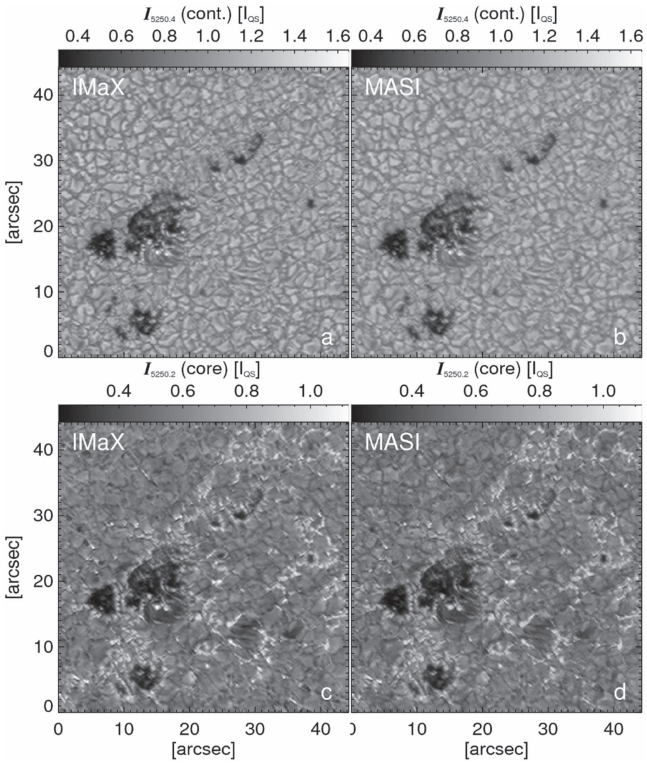


**Figure 10.** Stokes $I$ continuum (panel (a)) and line-core (panel (c)) image of the reconstructed IMaX observation and the degraded Stokes $I$ continuum (panel (b)) and line-core (panel (d)) image from the second-iteration MASI result.

The similarity between simulation and observation makes it possible to extend the merit function by a term that slightly reduces the demolition of the horizontal flow pattern and magnetic field lines by the re-sorting:

$$\chi^2 = CD + \frac{1}{32}\sum_{w=1}^{8}\sum_{s=1}^{4}\frac{(I_{w,s}^{\rm obs}(x_o, y_o) - I_{w,s}^{\rm syn}(x_m, y_m))^2}{\sigma_s^2}, \quad (2)$$

where $C$ is a constant that determines the strength of the correction term and

$$D = \sqrt{(x_o - x_m)^2 + (y_o - y_m)^2} \quad (3)$$

is the distance between the considered observed pixel and the synthetic one. The correction term, $C\,D$, gives a preference to synthetic pixels that are located close to the observed pixel. In our example we set $C = 0.004$ km$^{-1}$, which is a relatively small value, in order to prefer neighboring pixels only in the case that multiple synthetic pixels possess almost identical Stokes profiles. With this selection, 19% of the $812 \times 812$ entries in the archive of the second iteration provide the best-fit results used for the re-sorted data set.

Figure 10 contrasts the Stokes $I$ continuum and line-core image of the reconstructed IMaX observation with the degraded MASI result of the second iteration. Compared to the first iteration the agreement has slightly improved. Even the penumbra-like region does not show any obvious artifacts. A comparison of the observed Stokes profiles (reconstructed and corrected for the etalon blueshift) with the best-fit profiles resulted from the second MASI iteration can be seen in Figure 11. We selected three pixels located at the positions (13.″89, 26.″79), (17.″48, 39.″37), and (6.″43, 18.″35) in

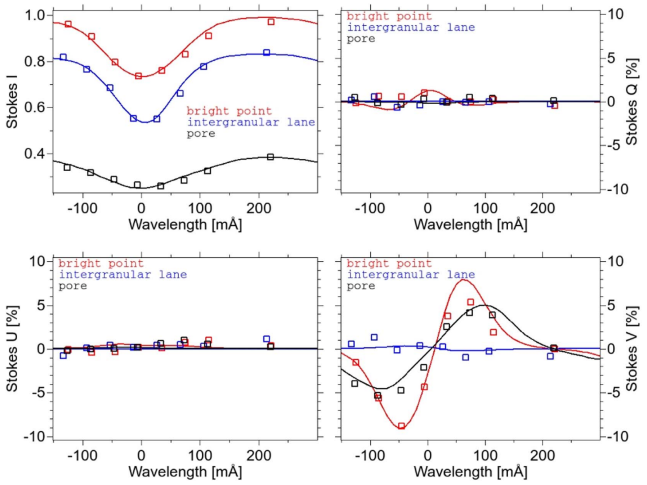


**Figure 11.** Stokes $I$, $Q$, $U$, and $V$ profiles from a position inside a bright point (red), an intergranular lane (blue), and a pore (black). The squares display the reconstructed and blueshift-corrected IMaX observation, while the solid lines correspond to the second MASI iteration, i.e., the best-fit inversion results. All profiles are normalized to the spatially averaged quiet-Sun intensity.

Figure 10, representing a bright point, an intergranular lane, and a pore. MASI provides for the three pixels a magnetic field strength at $\log(\tau) = -1$ of 1520 G, 205 G, and 2490 G, respectively. The kilogauss field in the pore and in the bright point broadens the spectral line. The low temperature gradient in the pore together with the temperature sensitivity of the Fe I 5250.2 Å line lead to a shallow Stokes $I$ profile. Since the magnetic field is weak for the intergranular-lane pixel, the corresponding polarization signals are also weak. The magnetic field of the pixel in the pore and the pixel in the bright point is strong and nearly vertical so that the Stokes $Q$ and $U$ signals are weak, while the Stokes $V$ profiles reach values of a few percent.

A look at the undegraded Stokes $I$ continuum image of the re-sorted MHD data set demonstrates the improvements of the second iteration even more distinctly. While the result of the first iteration show a wealth of small-scale discontinuities (see the left panel of Figure 12), this is rarely the case for the ouput of the second iteration (right panel of Figure 12).

The improvement of the inversion's quality can also be seen by a comparison of the $\chi^2$ maps. Panels (a) and (b) of Figure 13 show the total $\chi^2$ map of the second iteration decomposed into the distance term, $C\,D$, and the remaining Stokes part, $\chi^2_{IQUV}$. The Stokes part is further decomposed into the contribution of purely Stokes $I$ ($\chi^2_I$, panel (c) of Figure 13) and the remaining Stokes parameters ($\chi^2_{QUV}$, panel (d)), which allows a direct comparison of the $\chi^2$ components of the first iteration (panels (b)–(d) of Figure 8) with the ones of the second iteration (panels (b)–(d) of Figure 13). The maximum $\chi^2_{IQUV}$ value of the second iteration is 1.9 times lower than for the first iteration. The mean $\chi^2_{IQUV}$ value decreased from 17.1 to 7.9, the mean $\chi^2_I$ value from 10.9 to 5.8, and the mean $\chi^2_{QUV}$ value from 6.3 to 2.1. On average, the additional correction term, $C\,D$, contributes 34% to the total $\chi^2$ value, while 48% originate from Stokes $I$, and 18% from Stokes $Q$, $U$, and $V$ together.

Stokes $V$ maps in the red wing of the 525.02 nm line are displayed for the reconstructed IMaX observation and the degraded MASI result in Figure 14. The reconstructed IMaX

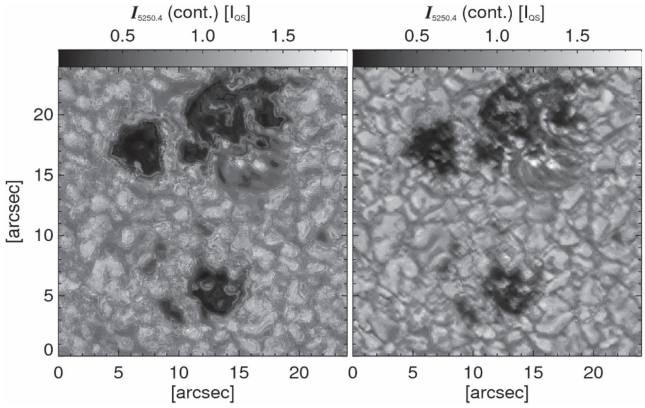


**Figure 12.** Undegraded Stokes $I$ continuum image after the first (left panel) and second (right panel) MASI iteration. Only the bottom left $24'' \times 24''$ part of the considered field of view is shown for a better visibility of details.

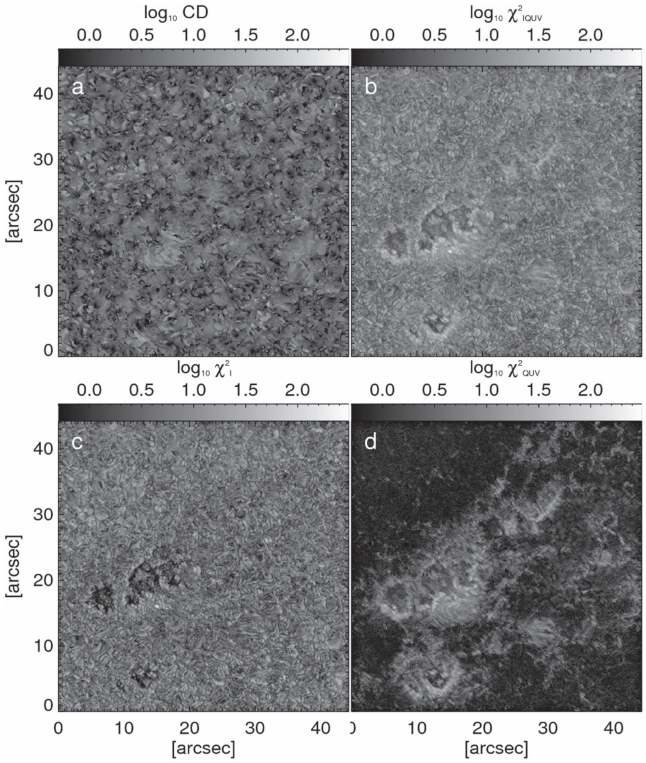


**Figure 13.** Contributions to the total $\chi^2$ values of the second iteration provided by the distance term in Equation (2) (panel (a)), by the sum of all four Stokes parameters (panel (b)), by only Stokes $I$ (panel (c)), and by the sum of Stokes $Q$, $U$, $V$ (panel (d)). All panels are plotted on a logarithmic scale.

Stokes $V$ image shows much more fine structure than the level-1 data (see left panel in Figure 7). Most of the fine structure is well reproduced by the second MASI iteration, although some features are not well fitted, largely the ones with a nearly horizontal magnetic field. Nonetheless, the discrepancy between observation and MASI at the position of the penumbra-like feature and also of the flux-emergence region is lower than for the first MASI iteration.

We consider some more undegraded quantities of the second MASI iteration in Figures 15 and 16.

Figure 15 compares maps of the LOS velocity between IMaX and MASI. Since a 25% global stray-light contamination is part of the MASI degradation, we applied a corresponding stray-light correction to the reconstructed IMaX data and fitted

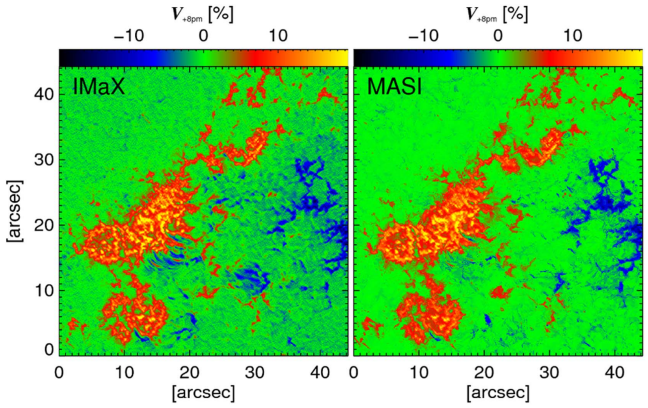


**Figure 14.** Normalized Stokes $V$ image at +8 pm offset from the line core. Left panel: reconstructed IMaX data. Right panel: degraded MHD data re-sorted by the second MASI iteration.

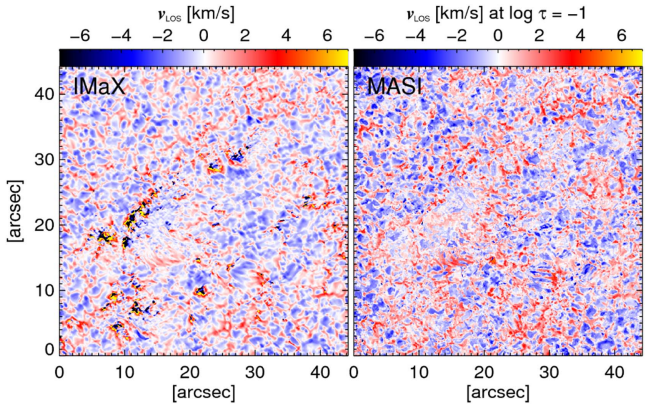


**Figure 15.** Map of the line-of-sight velocity. Left panel: classical estimate from the reconstructed data observed by IMaX (Stokes $I$ Gaussian fit). Right panel: undegraded MHD data at $\log(\tau) = -1$ re-sorted by the second MASI iteration. Negative velocities correspond to upflows.

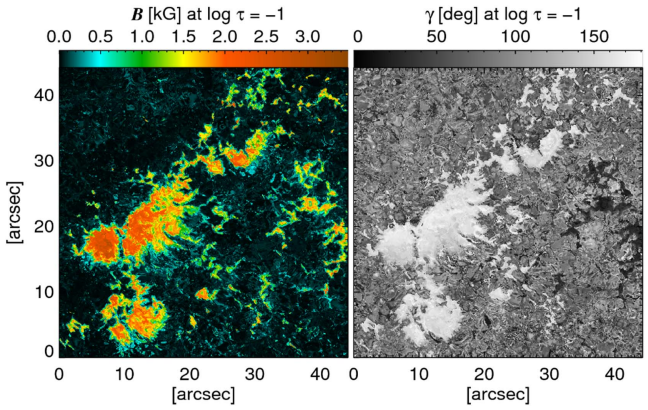


**Figure 16.** Magnetic field strength (left panel) and inclination (right panel) at $\log(\tau) = -1$, both taken from the undegraded second-iteration MASI result.

the Stokes $I$ profiles with a Gaussian. The central position of the Gaussian (corrected for the blueshift) provides the LOS velocities in the left panel of Figure 15. The right panel displays the vertical component of the re-sorted MHD velocity vector at the optical depth $\log(\tau) = -1$, because this depth is roughly the formation height of the 525.02 nm line. The velocity scale was shifted to reach a zero mean value over the entire FOV.

For both panels of Figure 15 the granulation outside the pores exhibits the typical upflows within granules and downflows for the intergranular lanes. The contrast of the MASI result is larger than that of the observation, possibly because the formation height of the 525.02 nm is somewhat higher than $\log(\tau) = -1$. For display reasons we limited the velocity range to $\pm 7\,\mathrm{km\,s^{-1}}$ because the Gaussian fits of the observed profiles have significant difficulties at the edges and inside the pores (see the black and yellow regions in the left panel of Figure 15). In the pores the temperatures are low and the temperature gradiants are small, both leading to shallow spectral lines. In combination with the photon noise the Gaussian fits can lead to unreasonable results.

Finally, we present the magnetic field of the second MASI iteration. The left panel of Figure 16 displays the field strength, while the right panel shows the field inclination, both at the optical depth of $\log(\tau) = -1$. In the pores we find field strengths up to 3400 G. We note that the MASI results hardly show any field weakening in the pores, which we mentioned in Section 4.2.4, which further indicates that our simplistic stray-light model is not too far off from reality.

## 5. Summary and Discussion

We obtained atmospheric parameters such as temperature, magnetic field vector, and LOS velocity from a spectro-polarimetric observation by finding the best-matched Stokes profiles from a snapshot of an MHD simulation, degraded as realistically as possible to the level of the observed data.

Because the MHD data set contains the full set of atmospheric parameters, we were able to re-sort the vertical columns of the original MHD data corresponding to the best fits of observational Stokes profiles and used the re-sorted data as the initial condition of a new MHD simulation. Since the spatial relations of the columns are destroyed (in the horizontal directions) by the re-sorting, the initial condition is physically inconsistent. The inconsistencies include the re-arranged horizontal flow pattern both above and below the solar surface, and the loss of local horizontal pressure balance, which are closely related to the convection in the granulation cells, so that the observed granulation pattern is destroyed immediately after the start of the MURaM continuation. The MURaM code is able to remove the physical inconsistencies, so that after about three minutes a new granulation pattern has evolved and after about half an hour of solar time the divergence of the magnetic field vector is brought down to zero. Further studies are needed to find ways to reduce the relaxation time, e.g., by carrying out more iterations or by advancing the applied merit function to preserve the horizontal flows of a granule in a statistical way (as we tried by adding the very simplistic distance term in Equation (2)).

After the relaxation we obtained physically consistent MHD simulations that show a solar scene quite similar to the observed one. We used a snapshot of the new simulations to apply a second iteration of the method. The higher similarity to the observation improved the match between observed and synthetic Stokes profiles. In particular, the improvement can be seen if undegraded Stokes images of the two iterations are compared and also by a significant decrease in the mean $\chi^2$ value and its contributions from Stokes $I$ and from Stokes $Q$, $U$, $V$, respectively.

The high computational effort needed for the MURaM simulations hindered the realization of further iterations within

this study, which are expected to lead to a stepwise convergence between observation and simulation, although it is clear that effects of an imperfect modeling of instrumental effects and imperfections of the MHD code (e.g., for penumbrae) cannot be lowered by more iterations.

The MASI technique can be understood as a first step toward an integration of the MHD equations into the Stokes inversion of a time series. Although we are still a long way away from this long-term goal, a few applications of the technique can already be considered:

1. By means of the MASI technique we are able to create MHD simulations that are very similar to an observation. This can be quite helpful in analyzing physical phenomena. For example, the MHD data allow for insights into all physical quantaties, even those that are not covered by the spectral lines (horizontal velocities, densities, pressures, horizontal force balance). It is also advantageous that the MHD data are free of noise and can have higher spectral, spatial, and temporal resolution. Moreover, the availability of an MHD simulation similar to the observation can be also quite useful in analyzing instrumental effects (e.g., the stray-light behavior).
2. The MASI method allows the creation of new MHD simulations with interesting solar targets, e.g., light bridges or complex sunspot or pore topologies, which was difficult in the past.
3. The MASI results after the first step can be used as a first-guess atmosphere for a traditional Stokes inversion technique so that the traditional inversion can converge faster.

Although the technique presented here is promising, this paper is limited to first steps and much work remains to be done to test and improve it further. A first important test could be a comparison between the MASI results and those of traditional inversion techniques. Ideally, this should be done with realistically degraded MHD data, because then the errors caused by the MASI technique can be disentangled from the errors made by traditional inversions, which would not be easy if observational data were inverted. Furthermore, it should be investigated whether more iterations lead to further improvements and, if so, how many iterations are needed until the $\chi^2$ values converge to their final value. An application of the MASI method to other observational data sets is also desirable, in particular to data with full line profiles (i.e., better spectral sampling) and a better knowledge of instrumental effects. Additionally, the MHD archive should be expanded by features harboring more horizontal fields (flux emergence, penumbrae) and local-dynamo simulations. Possibly the performance of MASI improves if the re-sorted MHD data are spatially smoothed (similar to the smoothing applied as part of the SPINOR inversion of the IMaX data, see Solanki et al. 2017) before being used as the initial condition of an MHD simulation. It also appears advisable to introduce Stokes-specific weighting factors in the merit function in order to reach a better balance between the contributions of the four Stokes parameters. Finally, an error estimate of the method should be derived, e.g., by considering all vertical columns of the original MHD data set that lead to very similar $\chi^2$ values.

The German contribution to SUNRISE and its reflight was funded by the Max Planck Foundation, the Strategic Innovations Fund of the President of the Max Planck Society (MPG), DLR, and private donations by supporting members of the Max Planck Society, which is gratefully acknowledged. The Spanish contribution was funded by the Ministerio de Economía y Competitividad under Projects ESP2013-47349-C6 and ESP2014-56169-C6, partially using European FEDER funds. The National Center for Atmospheric Research is sponsored by the National Science Foundation. The HAO contribution was partly funded through NASA grant number NNX13AE95G. The National Solar Observatory (NSO) is operated by the Association of Universities for Research in Astronomy (AURA) Inc. under a cooperative agreement with the National Science Foundation. This work was partly supported by the BK21 plus program through the National Research Foundation (NRF) funded by the Ministry of Education of Korea.

## References

Allende Prieto, C., Asplund, M., & Fabiani Bendicho, P. 2004, A&A, 423, 1109
Auer, L. H., House, L. L., & Heasley, J. N. 1977, SoPh, 55, 47
Barthol, P., Gandorfer, A., Solanki, S. K., et al. 2011, SoPh, 268, 1
Beck, C., Choudhary, D. P., Rezaei, R., & Louis, R. E. 2015, ApJ, 798, 100
Beck, C., Fabbian, D., Moreno-Insertis, F., Puschmann, K. G., & Rezaei, R. 2013a, A&A, 557, A109
Beck, C., Rezaei, R., & Fabbian, D. 2011, A&A, 535, A129
Beck, C., Rezaei, R., & Puschmann, K. G. 2013b, A&A, 549, A24
Berkefeld, T., Schmidt, W., Soltau, D., et al. 2011, SoPh, 268, 103
Berlicki, A., Heinzel, P., Schmieder, B., Mein, P., & Mein, N. 2005, A&A, 430, 679
Bianda, M., Solanki, S. K., & Stenflo, J. O. 1998, A&A, 331, 760
Borrero, J. M., Lites, B. W., Lagg, A., Rezaei, R., & Rempel, M. 2014, A&A, 572, A54
Buehler, D., Lagg, A., Solanki, S. K., & van Noort, M. 2015, A&A, 576, A27
Butterworth, S. 1930, Wireless Engineer, 7, 536
Carroll, T. A., & Kopf, M. 2008, A&A, 481, L37
Danilovic, S., Gandorfer, A., Lagg, A., et al. 2008, A&A, 484, L17
Danilovic, S., Schüssler, M., & Solanki, S. K. 2010, A&A, 513, A1
DeForest, C. E., Martens, P. C. H., & Wills-Davey, M. J. 2009, ApJ, 690, 1264
Frutiger, C. 2000, PhD Thesis No. 13896, ETH Zürich
Frutiger, C., Solanki, S. K., Fligge, M., & Bruls, J. H. M. J. 2000, A&A, 358, 1109
Gandorfer, A., Grauf, B., Barthol, P., et al. 2011, SoPh, 268, 35
Gonsalves, R. A., & Chidlaw, R. 1979, Proc. SPIE, 207, 32
Harvey, J., Livingston, W., & Slaughter, C. 1972, in Line Formation in the Presence of Magnetic Fields, ed. R. G. Athay, L. L. House, & A. Newkirk (Boulder, CO: HAO/NCAR), 227
Katsukawa, Y., & Orozco Suárez, D. 2012, ApJ, 758, 139
Lagg, A., Solanki, S. K., van Noort, M., & Danilovic, S. 2014, A&A, 568, A60
Lites, B. W., Akin, D. L., Card, G., et al. 2013, SoPh, 283, 579
Lucy, L. B. 1974, AJ, 79, 745
Martínez Pillet, V., del Toro Iniesta, J. C., Álvarez-Herrero, A., et al. 2011, SoPh, 268, 57
Mathew, S. K., Zakharov, V., & Solanki, S. K. 2009, A&A, 501, L19
Molowny-Horas, R., Heinzel, P., Mein, P., & Mein, N. 1999, A&A, 345, 618
Paxman, R. G., Schulz, T. J., & Fienup, J. R. 1992, JOSA, 9, 1072
Puschmann, K. G., & Beck, C. 2011, A&A, 533, A21
Puschmann, K. G., Ruiz Cobo, B., & Martínez Pillet, V. 2010, ApJ, 720, 141
Quintero Noda, C., Asensio Ramos, A., Orozco Suárez, D., & Ruiz Cobo, B. 2015, A&A, 579, A3
Rachkovsky, D. N. 1962a, IzKry, 27, 148
Rachkovsky, D. N. 1962b, IzKry, 28, 259
Rachkovsky, D. N. 1967, IzKry, 37, 56
Richardson, W. H. 1972, JOSA, 62, 55
Riethmüller, T. L., Solanki, S. K., Berdyugina, S. V., et al. 2014, A&A, 568, A13
Riethmüller, T. L., Solanki, S. K., van Noort, M., & Tiwari, S. K. 2013, A&A, 554, A53
Ruiz Cobo, B., & Asensio Ramos, A. 2013, A&A, 549, L4
Ruiz Cobo, B., & del Toro Iniesta, J. C. 1992, ApJ, 398, 375

Schüssler, M., Shelyag, S., Berdyugina, S., Vögler, A., & Solanki, S. K. 2003, ApJL, 597, L173
Socas-Navarro, H., de la Cruz Rodríguez, J., Asensio Ramos, A., Trujillo Bueno, J., & Ruiz Cobo, B. 2015, A&A, 577, A7
Socas-Navarro, H., Trujillo Bueno, J., & Ruiz Cobo, B. 2000, ApJ, 530, 977
Solanki, S. K. 1987, PhD Thesis No. 8309, ETH Zürich
Solanki, S. K. 1993, SSRv, 63, 1
Solanki, S. K., Barthol, P., Danilovic, S., et al. 2010, ApJL, 723, L127
Solanki, S. K., Riethmüller, T. L., Barthol, P., et al. 2017, ApJS, 229, 2
Tiwari, S. K., van Noort, M., Lagg, A., & Solanki, S. K. 2013, A&A, 557, A25
Tsuneta, S., Ichimoto, K., Katsukawa, Y., et al. 2008, SoPh, 249, 167
Tziotziou, K., Heinzel, P., Mein, P., & Mein, N. 2001, A&A, 366, 686
Unno, W. 1956, PASJ, 8, 108
van Noort, M. 2012, A&A, 548, A5
van Noort, M., Lagg, A., Tiwari, S. K., & Solanki, S. K. 2013, A&A, 557, A24
van Noort, M., Rouppe van der Voort, L., & Löfdahl, M. G. 2005, SoPh, 228, 191
Vögler, A., Shelyag, S., Schüssler, M., et al. 2005, A&A, 429, 335
Wedemeyer-Böhm, S. 2008, A&A, 487, 399